Experimental investigation of a turbulent natural convection flow in a cubic cavity with an inner obstacle partially heated

A. Weppe, F. Moreau, D. Saury

cite as:
A. Weppe, F. Moreau D. Saury, "Experimental investigation of a turbulent natural convection flow in a cubic cavity with an inner obstacle partially heated", International Journal of Heat and Mass Transfer, Volume 194 (September), 123052, 2022. DOI: 10.1016/j.ijheatmasstransfer.2022.123052

Experimental investigation of a turbulent natural convection flow in a cubic cavity with an inner obstacle partially heated

A. Weppe, F. Moreau, D. Saury

Institut Pprime, UPR CNRS 3346 - ISAE-ENSMA - Université de Poitiers, BP 40109 - 86961 Chasseneuil Futuroscope, France

Abstract

This work presents the dynamical and thermal behaviors of a turbulent natural convection flow occurring in a cubic cavity with an inner and partially heated obstacle. The top, bottom, front and back walls of the cavity are adiabatic and the other side walls are at imposed uniform temperature. Velocity and temperature measurements are carried out using Particle Image Velocimetry and micro-thermocouples. Boundary layer flows are observed in both vertical channels. A recirculating zone, in the upper part of the heated channel, breaks the linearity of the thermal stratification found in the lower part of the channel and it also disturbs heat transfers. A boundary layer instability of Tollmien-Schlichting type and the subsequent formation of an oscillating buoyant jet are analyzed. The presence of internal gravity waves in the thermally stratified heated channel are highlighted.

Email addresses: florian.moreau@ensma.fr (F. Moreau), didier.saury@ensma.fr (D. Saury)

Nomenclature

A	aspect ratio
f	frequency, Hz
g	gravitational acceleration, $m.s^{-2}$
H_{obs}	obstacle height (reference length), m
L	cavity length, m
$Nu(Z)$	local Nusselt number, $Nu(Z) = \frac{\partial\theta}{\partial Y} \times \frac{H_{obs}}{L}$
Pr	Prandtl number, $Pr = \nu/\alpha$
$Ra_{H_{obs}}$	Rayleigh number based on obstacle height, $Ra_{H_{obs}} = \frac{g\beta\Delta T H_{obs}^3}{\nu\alpha}$
Stk	Stokes number, $Stk = \frac{\rho d^2 v_{ref}}{18\mu l}$
S	stratification parameter, $S = \frac{\partial\theta}{\partial Z}$
T	temperature, K
T_0	reference temperature, $T_0 = \frac{1}{2}(T_h + T_c)$, K
U, V, W	dimensionless velocities (scaled by $\alpha\sqrt{Ra_H}$/H)
x, y, z	physical cartesian coordinates, m
X, Y, Z	dimensionless coordinates, $(X, Y, Z) = (x, y, z)/L$

Greek symbols

α	thermal diffusivity, $m^2.s^{-1}$
β	thermal expansion coefficient, K^{-1}
ΔT	temperature difference between the isothermal walls, $\Delta T = T_h - T_c$, K
ε	emissivity
θ	dimensionless temperature, $\theta = (T - T_0)/\Delta T$
λ	thermal conductivity, $W.m^{-1}.K^{-1}$
μ	dynamic viscosity, $kg.m^{-1}.s^{-1}$
ν	cinematic viscosity, $m^2.s^{-1}$
ρ	density, $kg.m^{-3}$
σ_X	standard deviation, *(units of X)*
Φ_X	power spectral density, *(units of X)*$^2.Hz^{-1}$
Ω	dimensionless pulsation

Subscripts and superscripts

bv	Brunt-Väisälä
c	cold
h	hot
obs	obstacle
ref	reference value
X'	X fluctuation ($X' = X_i - X$ where X_i is an instantaneous quantity and X is its time averaged value)

Abbreviations

DHC	Differentially Heated Cavity

1. Introduction

Natural convection in closed and confined spaces takes place in a wide variety of industrial configurations : ranging from a car's underhood to the cooling system of nuclear power plants. Within this range of specific designs, the high Rayleigh numbers often encountered lead to turbulent regimes. Numerical simulations, usually carried out in industrial context with RANS models to achieve adapted computation time, crudely lack of accuracy in the determination of the flow and the heat transfers. The case of enclosed cavities with obstacle is often encountered in actual applications. However, turbulent phenomena, occurring in such a situation, remain challenging. In order to tackle these issues, a simplified configuration is defined which allows to analyze natural convection flows being representative of flow regimes encountered in industrial contexts and especially in the underhood of cars. In this study, a cubic and partially heated obstacle is placed into a cubic enclosure. As it will be later depicted in the results section of the paper, the flow inside the heated channel has some similarities with both flows along vertical heated plates and differentially heated cavity flows.

Natural convection along a vertical heated plate has been first investigated theoretically and experimentally by Schmidt et al. [1] in laminar regime. Ostrach [2] specified the theory and compared it to experiments for various Prandtl numbers. A boundary layer type flow is found for Grashof numbers large enough and correlations for heat transfers are determined. When the Grashof number is increased up to a critical value along the heated vertical plate, the flow can become unsteady. Dring and Gebhart [3] highlighted a

filtering frequency mechanism discussed later in this paper. The unsteady flow will eventually lead to turbulence (Jaluria et al. [4]).

Turbulent flows inside differentially heated cavities (DHC) have also been studied both numerically and experimentally. For instance, Mergui et al. [5] or Salat et al. [6] investigated a cubic differentially heated cavity of Rayleigh number up to $Ra = 5.34 \times 10^9$. A separated boundary layers flow is observed. More recently, Belleoud et al. [7, 8] investigated a differentially heated cavity with aspect ratio $A \approx 4$ (cavity's height over cavity's width) for Rayleigh number based on the cavity height $Ra = 1.2 \times 10^{11}$. Turbulent quantities have been analyzed and compared with numerical results (Trias et al. [9]) with good agreements. The influence of an obstacle inside an enclosure was mostly studied numerically. House et al. [10] studied the effect of an obstacle conductivity and length in a DHC. They found that, for obstacle sizes large enough but not too large, heat transfers are decreased (respectively enhanced) in the enclosure when the ratio of the obstacle conductivity over the fluid conductivity is large (respectively small). Bhave et al. [11] studied the impact of a centered adiabatic obstacle inside a DHC and looked for an obstacle size where heat transfers are optimized. For $Pr = 0.71$ heat transfer can be increased by 4% when the ratio of the obstacle area over the cavity area is near the size of the existing stagnant core of the cavity without obstacle. Other cavity shapes as, for instance, E-enclosure [12] or H-shaped cavities [13] have been investigated using ISPH numerical methods. Liu and Phan-Thien [14] investigated more specifically the radiation effect of a heated obstacle in a DHC. The wall emissivity ϵ can play an important role on heat transfers ; the part of thermal radiation over the total heat transfer can reach 30% when $\epsilon = 0.9$ and the obstacle is sufficiently heated. Ha and Jung [15] pinpointed 3D effects when studying the conjugate heat transfer of a heated and conducting obstacle inside a DHC. Variation of the local Nusselt Number along the transverse direction are highlighted and induced by the conducting obstacle. Those numerical studies are still limited to laminar flow. The lack of experimental studies analyzing turbulent heat and fluid flows within an enclosure including an obstacle is a clear motivation for the present paper.

2. Experimental set-up

2.1. Cavity description

The setup consists in a partially side-heated cubic obstacle (referred later as "obstacle") of length $H_{obs} = 0.80\,\mathrm{m}$ centered inside a cubic cavity (referred

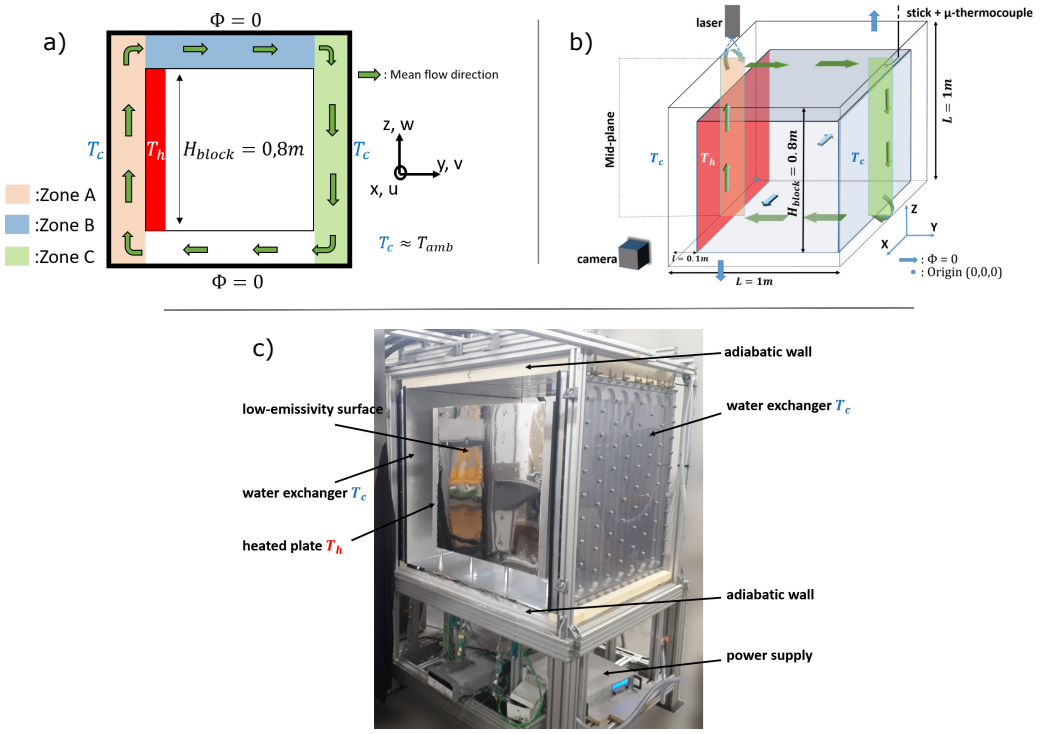

FIGURE 1 – a) 2D scheme of the experimental set-up and of the mean flow. b) 3D scheme of the experimental set-up and of the mean flow. c) Picture of the experimental set-up

later as "cavity") of inner edge length $L = 1.00\,\mathrm{m}$ (see Fig. 1.a and 1.b). In such a geometry, a distance $l = 10\,\mathrm{cm}$ between the inner obstacle and the surrounding cavity is then achieved.

The cavity walls are either isotherm or adiabatic. Two heat exchangers in aluminium (conductivity : $\lambda = 174\ \mathrm{W.m^{-1}.K^{-1}}$, emissivity : $\epsilon = 0.10$) impose a temperature $T_c = T_{amb}$ on two vertical cavity side walls (see Fig. 1.c) thanks to thermostated baths. The top and bottom horizontal walls of the cavity are made of 10 cm-thick extruded polystyrene ($\lambda = 0.035\,\mathrm{W.m^{-1}.K^{-1}}$) and are then considered as adiabatic. They are also covered with low-emissivity aluminum sheets ($\epsilon = 0.08$) to minimize the radiation effects. The front and rear walls of the cavity are 6 mm-thick glass panels which enable flow visualization. Extruded polystyrene blocks are maintained in front of the glass panels to keep them thermally insulated. A window is preserved for flow visualization and measurements.

The inner partially heated obstacle is held by four polymer rods which re-

duce conduction heat transfer ($\lambda = 0.25\,\mathrm{W.m^{-1}.K^{-1}}$). They are placed at each obstacle ends to limit flow disturbances in the mid-depth plane where measurements are carried out. The obstacle is made up of two 4 cm-thick aluminium plates ($\lambda = 174\,\mathrm{W.m^{-1}.K^{-1}}$). One of the plate is heated by a heating wire at $T_h = T_c + \Delta T$. Those two plates are the obstacle side walls which are in front of the cavity side walls maintained at T_c. Between those two plates are a Rockwool panels succession along with Ertalon and POM-C plates. The temperature is thus decreasing from the heated plate up to the other obstacle side wall. That other wall preserves the whole mechanical strength. Front, rear, top and bottom walls are covered with 4 mm POM-C plates keeping good surface condition. Those plates are also covered with low-emissivity aluminum sheets ($\epsilon = 0.08$).
The temperature difference between the heated plate of the inner obstacle and the cavity side wall is maintained at $\Delta T = T_c - T_f = 32\,\mathrm{K}\pm0.3\,\mathrm{K}$. This is the temperature difference between those two vertical isothermal plates that creates air motion inside the cavity. A Rayleigh number, based on the height H_{obs} of the inner obstacle used in this study is $Ra_{H_{obs}} = \frac{g\beta\Delta T H_{obs}^3}{\alpha\nu} = 1.37(\pm0.1)\times10^9$, with α the thermal diffusivity, ν the kinematic viscosity and β the compressibility coefficient. x,y and z axis are made dimensionless with respect to L.

Note that the ambient temperature in the experimental hall, isothermal plate temperatures of the cavity (imposed by the two thermostated baths) as well as the temperature of the 6 surfaces of the inner obstacle are continuously monitored to ensure suitable and well-known boundary conditions. 1 Pt100 probe and 69 type-K thermocouples are calibrated and used for this purpose. Data are recorded via a data acquisition unit agilent 34972A at a frequency of $\frac{1}{60}$ Hz.

2.2. Velocities measurements

Velocities were measured using PIV (Particle Image Velocimetry) measurement technique. A smoke generator produces particles used as the flow tracers. Those tracers are paraffine oil particles with a diameter $d \approx 5\,\mu\mathrm{m}$ leading to a Stokes number $Stk = \frac{\rho_p d^2 v_{ref}}{18\mu l} = 6.2\times10^{-4}$ where ρ_p is the density, μ is the dynamic viscosity and $V_{ref} = \frac{\alpha}{H_{obs}}\sqrt{Ra_{H_{obs}}}$ is a typical scale velocity for natural convection [16]. The particles can be considered as good air tracers for natural convection flow since $\frac{V_g}{V_{max}} \approx 1.5\times10^{-3}$ where

$V_g = \frac{d^2 g(\rho_p - \rho_{air})}{18\mu}$ is the settling velocity and V_{max} is the maximum velocity encountered in the flow. The laser sheet is generated by a pulsed Nd:YAG laser (2×50 mJ@100Hz). The particles are visualized with a CMOS camera, $2560 \times 2160\,\text{pixels}^2$ (Fig. 2). The pixel pitch size is 7 µm and the field size is $120 \times 105\,\text{mm}^2$. 5000 pairs of images are acquired at 25 Hz and the time between two frames is ranging between 1000 µs and 8000 µs depending on the zone analyzed and the associated velocity of the flow. Image processing is carried out with LaVision PIV algorithm to obtain velocity vectors. The algorithm proceeds with interrogation area size ranging from 64×64 to 32×32 pixels^2 with 50% of overlapping. For each zone, statistics over the vertical and horizontal velocities are analyzed. The components (U, V, W) of the velocity are made dimensionless with respect to V_{ref} previously defined. See table 1 for the velocity uncertainty.

2.3. Temperature measurements

Temperature measurements were carried out in the vertical mid-depth plane at $X = 0.50$ with a type K micro-thermocouple (diameter = 12.7 µm). The cold junction is placed inside an aluminium block of large inertia. This block is placed in the experimental hall at $T = T_{amb}$ and its temperature is regularly measured with a PT100 probe (± 0.1 K). This type-K thermocouple is mounted on two pins of 100 µm joined on a rod, out of the vertical mid-depth plane ($X = 0.50$) in order to minimize the intrusive effects (Fig. 3). For the same reasons, this rod is placed downstream of the flow and 45° oriented regarding the flow direction. A displacement device allows the rod to move along the Y and Z axes with a 100 µm increment (± 6.5 µm). For each measurement, the acquisition frequency is set at 6 Hz and the acquisition time is 10 minutes to ensure statistical convergence. Moreover, the micro-thermocouple cut-off frequency is 20 Hz which is one order of magnitude greater than the maximum flow frequency. The temperature measurements are presented in terms of $\theta = \frac{T - T_0}{\Delta T}$ where $T_0 = \frac{T_h + T_c}{2}$ is the reference temperature.

Uncertainties for both the temperature and velocity are reported in the following table :

$u(\theta)$	$u(W)$
± 0.038	± 0.004

TABLE 1 – Velocity and temperature uncertainties

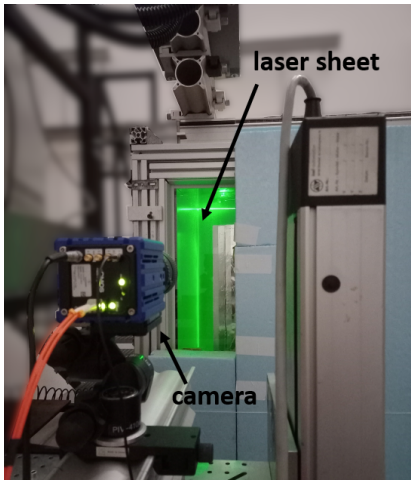

FIGURE 2 – PIV set-up

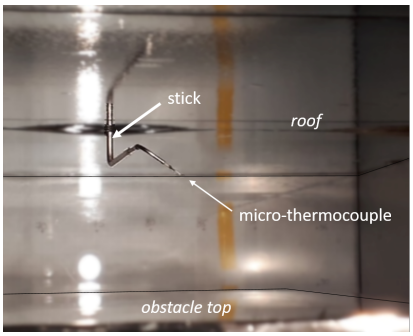

FIGURE 3 – Temperature measurement set-up

2.4. Heat fluxes measurements

Heat fluxes are locally measured on the heated plate at $T = T_h$ and the cavity side wall at $T = T_c$ in the vertical mid-depth plane at $X = 0.50$. They are quantified using the wall Nusselt number which corresponds to the dimensionless temperature gradient at the wall :

$$Nu = \frac{H_{obs}}{L} \times \left.\frac{\partial \theta}{\partial Y}\right|_{wall} \tag{1}$$

In order to compute the Nusselt number, the micro-thermocouple is progressively moved away from the wall by 100 µm increments until a maximum distance from the wall of 800 µm in order to remain into the linear zone of the temperature profiles. For each position, a temperature acquisition is made at a frequency of 40 Hz and an acquisition time of 10 minutes. The Nusselt number is then determined with the slope of the curve at the origin obtained by ANOVA on at least 5 points. A Nusselt number is validated only when the correlation coefficient on the slope exceeds $R^2 > 0.995$. The confidence interval at 95% is then computed using the Student's law (n being equal to the number of considered points and $n \geq 5$) :

$$Nu - t_{0.025,n-2}\sqrt{\frac{\hat{\sigma}^2}{D_{xx}}} \leq Nu \leq Nu + t_{0.025,n-2}\sqrt{\frac{\hat{\sigma}^2}{D_{xx}}}$$
$$\text{with} \quad D_{xx} = \frac{1}{{H_{obs}}^2}\sum_i (Y_i - \bar{Y})^2 \; ; \; \hat{\sigma}^2 = \frac{1}{n-2}\sum_i (\theta_i - \hat{\theta}_i)^2 \tag{2}$$

where $t_{0.025,n-2}$ is the quantile of order 97.5% for n-2 degrees of freedom of the Student's law, $\hat{.}$ and $\bar{.}$ refer respectively to the estimator and the mean.

3. Results

3.1. Dynamical behavior of the flow around the cavity

Velocity measurements were carried out in the vertical mid-depth plane (at $X = 0.5$). The setup is divided into three zones in order to facilitate its description (see Fig. 1.a) :

— Zone A : the vertical differentially heated channel ($X = 0.5$, $Y \in [0; 0.1]$ and $Z \in [0; 1]$)

— Zone B : the top horizontal channel ($X = 0.5$, $Y \in [0.1; 0.9]$ and $Z \in [0.9; 1]$)

— Zone C : the vertical unheated channel. ($X = 0.5$, $Y \in [0.9; 1]$ and $Z \in [0; 1]$)

The dynamical behavior of the flow will be analyzed in the following sections via dimensionless velocity fields and horizontal or vertical dimensionless velocity profiles around the cavity.

3.1.1. Velocity measurements in the heated channel (Zone A)

A developing boundary layer flow along the hot plate at temperature T_h can be observed in zone A (Fig. 4). In Fig. 5, the profiles of W, the vertical component of the mean velocity, show that the maximum velocity, located inside the boundary layer, as well as the thickness of this layer increase with Z. When the flow reaches $Z = 0.9$, it divides into two parts. It either flows into the top horizontal channel (zone B), or towards the cold plate at T_c. There, the flow can either go downward along the cold plate where a boundary layer is developing, or join the top recirculation area (Fig. 4). It is worth mentioning that the recirculation area at the top of the zone A will be of primary importance regarding the thermal analysis that will be discussed later in section 3.2.1.

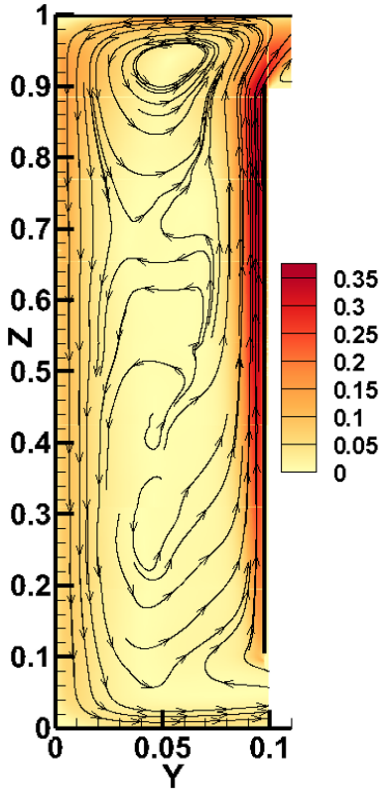

FIGURE 4 – Norm of the mean dimensionless velocity field and streamtraces (→) for zone A

At $Z = 0.893$ and $Y > 0.08$ (end of the hot boundary layer), positive values of the horizontal component of the mean velocity V, observed on the profile (see Fig. 5 (right)), exhibit the onset of the deviation of the mean jet flow towards the horizontal channel observed in the top part of the zone A ($Z > 0.9$, Fig. 4). The profile of the vertical component of the mean velocity W, at $Z = 0.5$ (Fig. 5 (left)), depicts well the developed boundary layers along both the hot and cold plates. They do not have the same intensity as the absolute maximum velocity into the cold boundary layer is more than three times less than the one in the hot boundary layer ($W_{cmax} = 0.10$ compared to $W_{hmax} = 0.32$). As already outlined, it is because a part of the heated flow goes into zone B, thus breaking the flow symmetry. When the descending flow reaches $Z = 0.1$, it can either fuel the forming hot boundary layer, or flow into the lower horizontal channel. There is also a flow coming

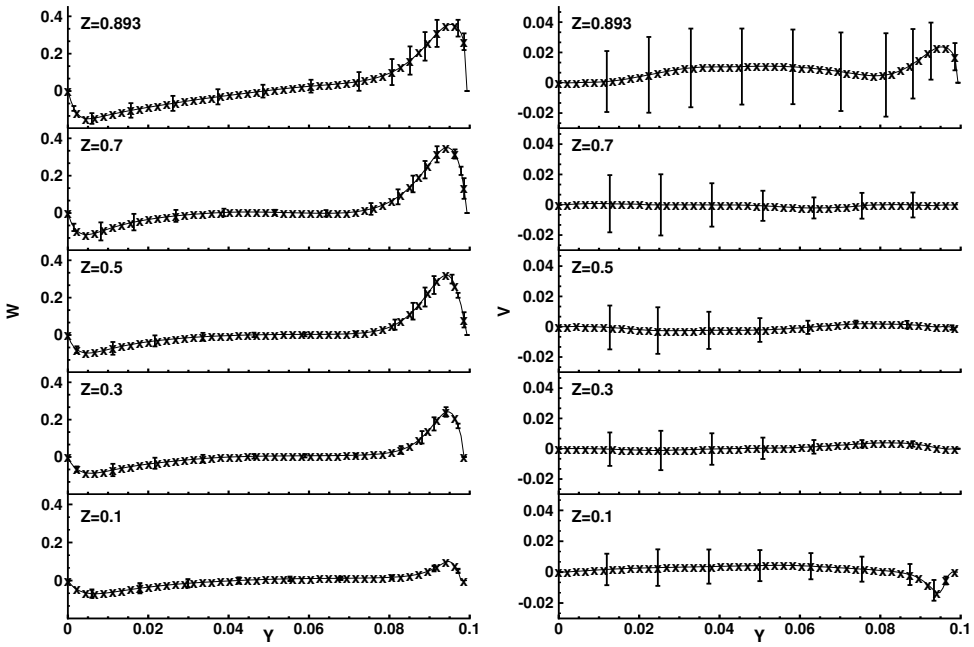

FIGURE 5 – Vertical (left) and horizontal (right) mean dimensionless velocity profiles along the cavity (zone A). Vertical bars (I) are of length $2\sigma_w$ (left) or $2\sigma_v$ (right). Please note the different vertical scales.

from the lower horizontal channel and following the developing hot boundary layer. This flow comes from the mean flow depicted in figure 1.a. At $Z = 0.1$, the profiles of the horizontal (V) and vertical (W) mean velocity components show the origin of the boundary layer flow observed along the hot plate. An incoming horizontal flow (V<0) coming from the lower channel feeds the vertical developing hot boundary layer and induces a thicker boundary layer in that area. Note that it is then a rather different case from the boundary layer theory assuming a zero velocity near the leading edge of the heated vertical plate. In the end, it comes out that there is a weak interaction between the hot and cold boundary layers into the majority of zone A. In fact, the profiles of the horizontal component, V, of the mean velocity are close to 0 all along the cavity for $0.1 < Z < 0.8$.

The RMS velocity fluctuations are quantified in figure 5 via the vertical bars. Most of the vertical velocity fluctuations are located inside the boundary layers with greater values in the hot boundary layer. On the contrary, the fluctuations of the horizontal velocity are mostly near the outer cold boun-

dary layer. It shows that the cold boundary layer fluctuates more horizontally than the hot one. At $Z = 0.893$, the fluctuations of the horizontal velocity are greater all along Y because of the recirculation area effects.

3.1.2. Velocity and temperature measurements in the horizontal channel (zone B)

As described in zone A, a part of the flow leaving the hot side of the obstacle goes to the top horizontal channel (Fig. 6). The horizontal mean

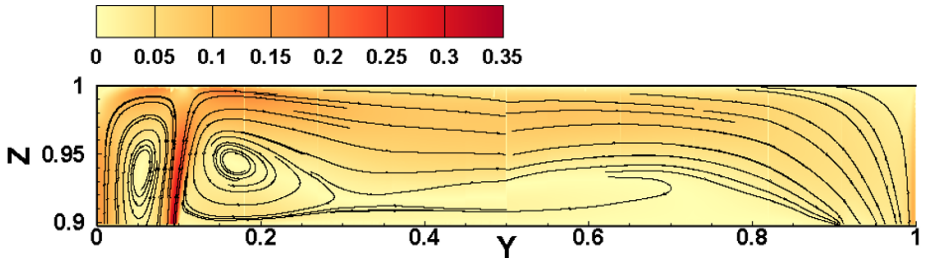

FIGURE 6 – Norm of the mean dimensionless velocity field and streamtraces (→) for zone B as well as upper parts of zones A and C.

velocity profiles at $Y = 0.15$ (Fig. 7) show an horizontal wall jet along the upper wall of the cavity. From $Y = 0.15$, this wall jet thickens until the middle of the channel ($Y = 0.5$) and its maximum velocity decreases. Figure 6 shows a very low velocity zone from $Y = 0.5$ to $Y = 0.8$ next to the upper face of the obstacle. In this range, the horizontal mean velocity profiles next to the upper face of the obstacle display flat shapes. A clockwise-rotating recirculation area, fueled by the later described oscillating buoyant jet, drives the flow near to the upper face of the obstacle from $Y \approx 0.3$ to lower values of Y. It results, in that area, in a reversal wall flow (see Fig. 7, $Y = 0.25$).

Regarding the temperatures, it can be observed that the profiles are quite flat for most Z and all along the top horizontal channel. Upstream, at $Y = 0.15$ and at the upper face of the obstacle ($Z \approx 0.90$), a non-adiabatic behavior for the temperature profile can be observed. This is caused by the proximity of the vertical heated plate (located at $Z = 0.90$ and $0.10 \leq Y \leq 0.14$). Downstream, at $Y = 0.85$, a similar observation can be made, the flow going to the vertical unheated channel (zone C) gets close to the unheated aluminium plate (located at $0.86 \leq Y \leq 0.90$ and $Z = 0.90$). As it is hotter than the plate, a heat exchange between the fluid and the plate occurs at this location. In other locations ($Y = 0.25$, $Y = 0.50$ or $Y = 0.75$),

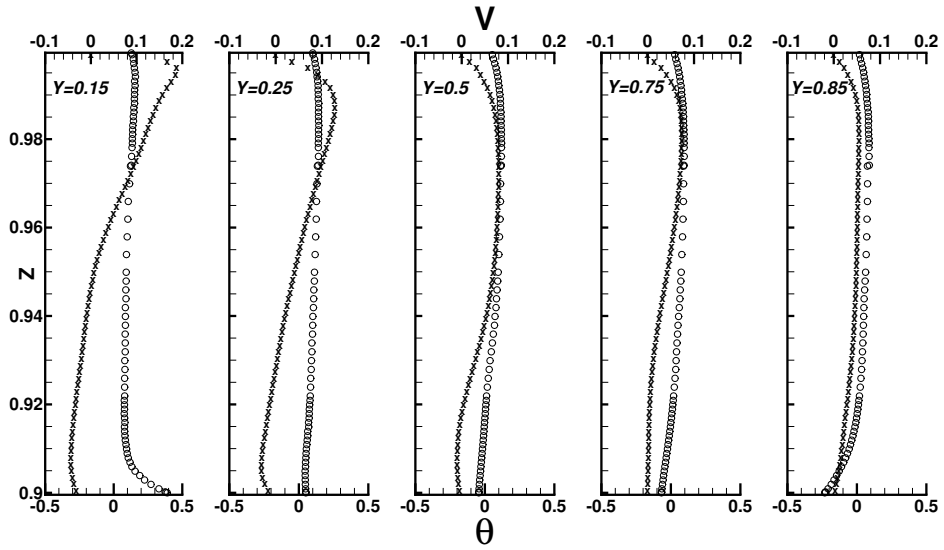

FIGURE 7 – Mean horizontal dimensionless velocity and mean dimensionless temperature profiles for zone B ; θ ($\circ$) ; V ($\times$)

wall temperature profiles ($Z = 0.90$ or $Z = 1$) exhibit a behavior which is close to the typical one observed in the vicinity of adiabatic surfaces.

3.1.3. Velocity measurements in the unheated channel (Zone C)

The mean velocity field (Fig. 8) shows the path of the flow coming from the top horizontal channel (Zone B).

At the top of the zone C ($Z \in [0.90; 1]$), the flow coming from zone B, either goes towards the vertical plate maintained at T_c (at $Y = 1$), or flows back to the obstacle side (at $Y = 0.90$). In fact, at this elevation, both surfaces are colder than the flow (as it will be detailed later, in section 3.2.2). It results in a descending wall flow along both plates. At $Z = 0.893$, the profile of the horizontal component, V, of the mean velocity (Fig. 9) exhibits positive values, which confirms that the whole flow entering in zone C is coming from the top horizontal channel.

It also results in RMS fluctuations at this elevation which are significant. The vertical component, W, of the mean velocity in the upper part of the channel ($Z > 0.50$) confirms the development of two descending vertical boundary layers although the maximum velocity in the boundary layer at the cavity cold plate, at T_c, is three times greater than the one at the obstacle's

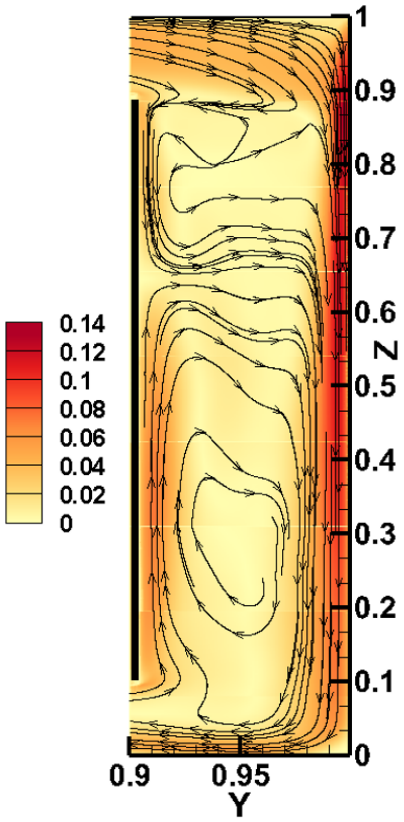

FIGURE 8 – Norm of the mean dimensionless velocity field and streamtraces (→) for zone C

side. Actually, it keeps part of its momentum from the top horizontal channel. This boundary layer has a quite similar trend as the cold boundary layer of zone A. It looses velocity and thickens as Z decreases. The flow deviates to the bottom horizontal channel when it reaches $Z < 0.10$. In figure 8, it can be observed that the boundary layer behavior on the obstacle's side ($Y \approx 0.9$) differs considerably. The flow is descending along the obstacle side until $Z \approx 0.65$ where it impinges an ascending vertical boundary layer flow. In the impact area ($Z \in [0.60; 0.70]$), the flow leaves the wall horizontally and goes through the central zone to join the cold plate of the cavity and its developing boundary layer. This direction change is located at the elevation where the obstacle boundary layer flow has the same temperature as the central zone (see section 3.2.2). For $Z \in [0.10; 0.65]$, the flow is ascending

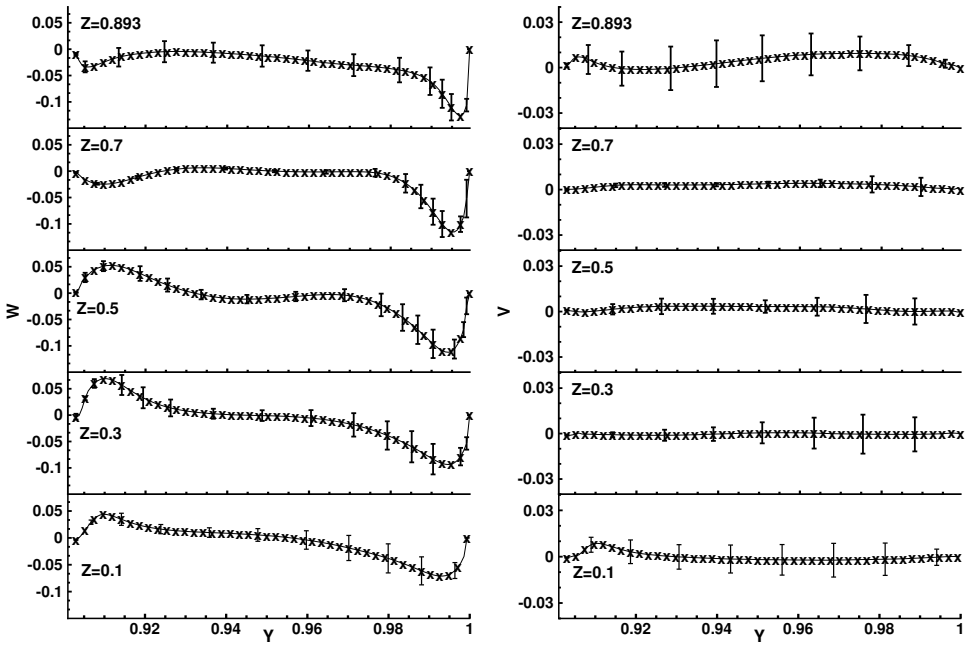

FIGURE 9 – Vertical (left) and horizontal (right) mean dimensionless velocity profiles along the cavity (zone C). Vertical bars (I) are of length $2\sigma_w$ (left) or $2\sigma_v$ (right). Please note the different vertical scales.

along the obstacle. The boundary layer is in fact fuelled by both a cold reversed flow from the bottom horizontal channel and the flow coming from a recirculating zone observed in the lower part of the channel. This recirculating zone is formed by the temperature difference between the cold plate and the obstacle for $Z < 0.65$.

3.2. Thermal behavior

3.2.1. Thermal stratification and heat transfers (Zone A)

Temperature profiles into the heated channel have been plotted in figure 10 for several elevations.

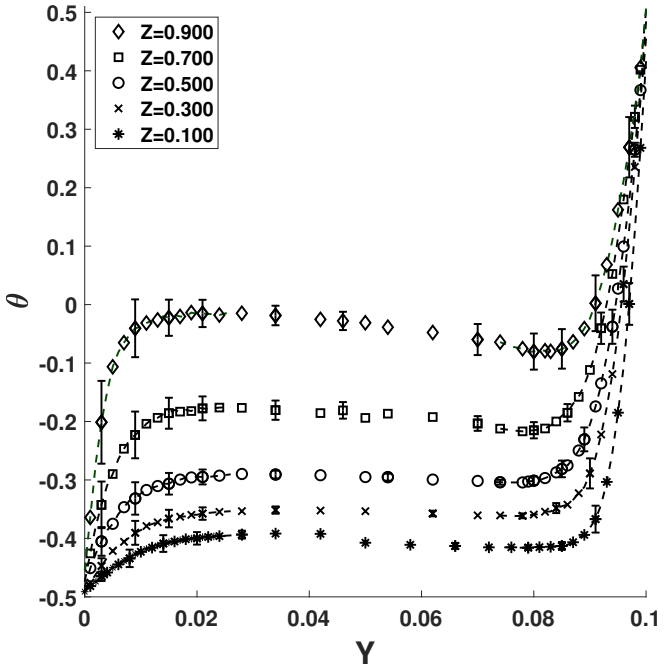

FIGURE 10 – Mean dimensionless temperature profiles for different Z in zone A. Vertical bars (I) are of length $2\sigma_\theta$.

Firstly, these profiles depict that thermal boundary layers are developing on both the cold and hot plates constituting this vertical differentially heated channel. Secondly, the temperature increases in the core zone as Z increases. The central zone is stratified in temperature. Focusing on this variation, the mean temperature profile along the vertical central line, $X = 0.50$ and $Y = 0.05$, were plotted in figure 11.

The evolution is linear for $Z \in [0.10; 0.50]$. The stratification parameter $S(Z) = \left.\frac{\partial\theta}{\partial Z}\right|_{Y=0.05}$, which is the vertical temperature gradient in the linear zone ($[0.10; 0.50]$), is equal to $S = 0.29$. This value is surprisingly lower than common values obtained for differentially heated cavity (see Belleoud [8] for

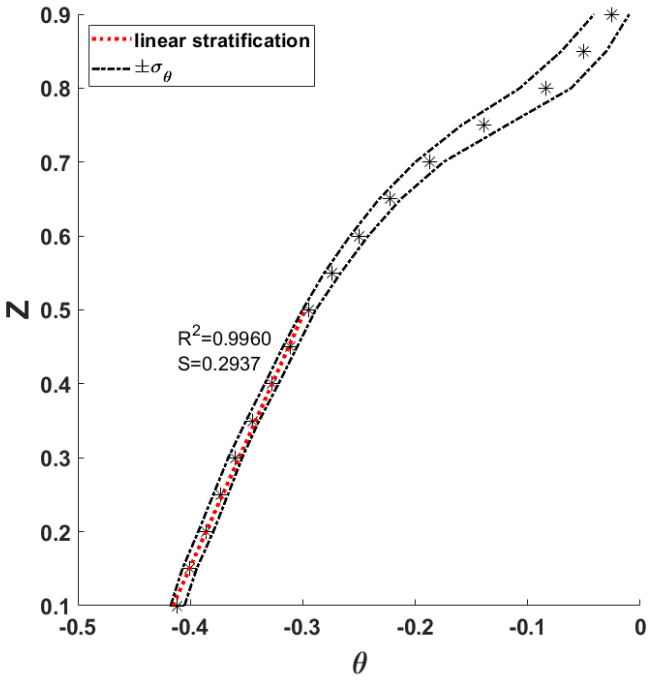

FIGURE 11 – Vertical profile of the mean dimensionless temperature at $Y = 0.05$

instance). Actually, as previously explained, a part of the hot flow leaves zone A (the heated channel) to zone B (top horizontal channel) rather than going towards the cold plate as it is the case for a closed cavity. It results in a lower increase of temperature into the core of zone A. The vertical temperature gradient, $\frac{\partial\theta}{\partial Z}(Z)$, increases substantially from 0.29 for $Z \in [0.10; 0.50]$ to 0.70 for $Z \in [0.50; 0.80]$. This trend is explained by the growing influence of the top recirculation area on the core flow as Z increases. The linear variation of the stratification is thus broken. Due to the recirculation area, the temperature fluctuations quantified by σ_θ are also greater as Z increases.

In order to study the heat transfer in zone A, Nusselt numbers (Eq. 1) as well as associated confidence interval (Eq. 2) were measured along the hot and cold plates (respectively Figs. 12 and 13).

Along the hot plate ($Y = 0.1, Z \in [0.10; 0.90]$), the Nusselt number is strictly decreasing when Z increases (see Fig. 12). Indeed, the hot boundary layer thickens and the fluid heats up. It results in a diminution of the heat transfer with the plate. At $Z < 0.20$, the Nusselt spatial variations are steeper

due to the twofold influence of the cold flows coming from both the cold plate and the lower horizontal channel (see Fig. 4). Thus, the temperature difference is highly increased and so are the heat transfers. The fluctuations of the Nusselt number at $Z \geq 0.80$, are probably due to the disturbances coming from the cold flow driven by the top recirculation area.

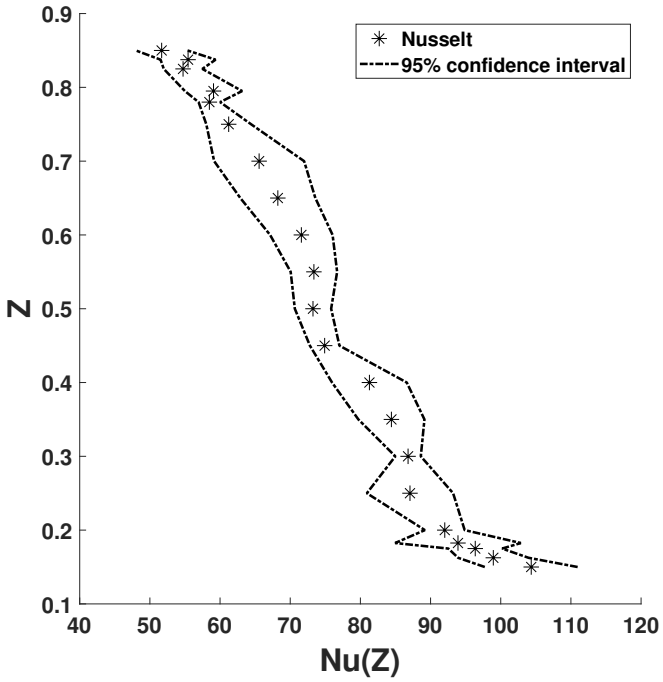

FIGURE 12 – Nusselt numbers along the heated vertical plate (Zone A, $Y = 0.1, Z \in [0.10; 0.90]$, $X = 0.50$)

The Nusselt numbers on the cold plate at T_c ($Y = 0, Z \in [0; 1]$) (Fig. 13) are decreasing when Z decreases. Indeed, the temperature difference between the plate and the fluid reduces : the fluid cools down as it flows downward and thus the heat transfers decrease. This decrease is steeper for $Z \in [0.55; 0.70]$; This trend is explained by the influence of the top recirculation area (for $Z \geq 0.6$, see Fig. 4).

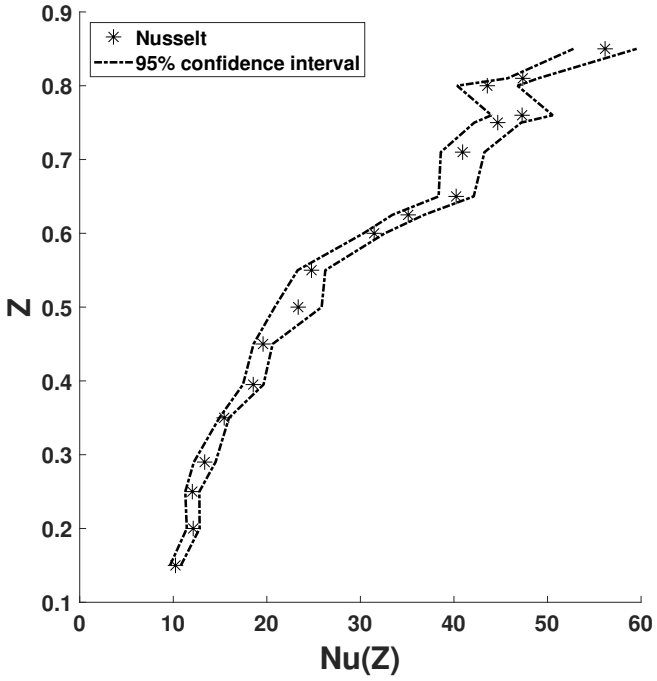

FIGURE 13 – Nusselt numbers along the cold plate (Zone A, $Y = 0, Z \in [0; 1]$, $X = 0.50$)

3.2.2. Temperature measurements (Zone C)

Horizontal profiles of temperature in the unheated channel have been plotted in figure 14. A thermal boundary layer is developing along the cold plate at T_c ($Y = 1, Z \in [0; 1]$). Its thickness tends to increase. On the other side ($Y = 0.90, Z \in [0.1; 0.9]$), two opposite wall flows are observed (Fig. 8) and are strongly connected with the temperature difference between the fluid and the wall (Fig 14).

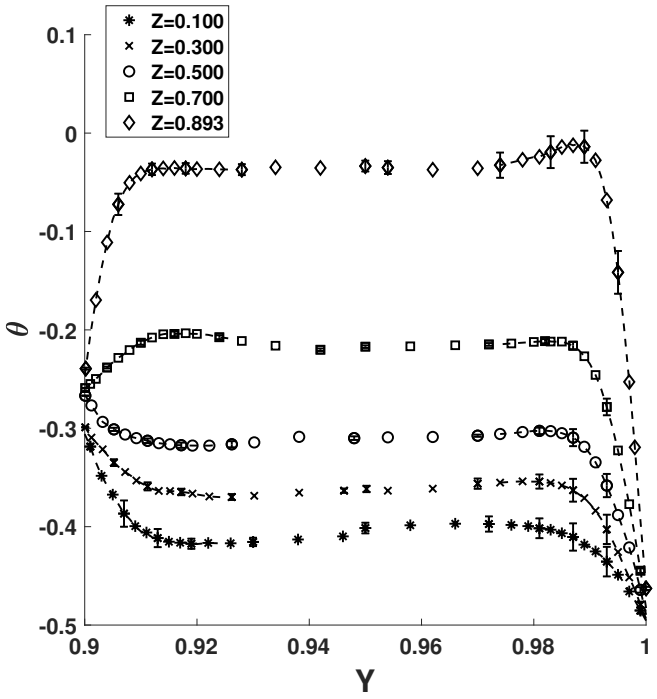

FIGURE 14 – Mean dimensionless temperature profiles for different elevations, Z, in zone C. Vertical bars (I) are of length $2\sigma_{w,v}$.

At $Y = 0.90$ and for $Z = 0.89$ and $Z = 0.70$, a boundary layer-like temperature profile can be observed with the fluid being hotter than the obstacle. On the contrary, for $Z = 0.50$, $Z = 0.30$ and $Z = 0.10$, a boundary layer-like temperature profile develops with the fluid being colder than the obstacle. In fact, a part of the flow coming from the upper horizontal channel cools down along the wall of the obstacle. When it reaches the temperature of the obstacle (for $Z \in [0.50, 0.70]$) it heads towards the colder plate (at T_c and $Y = 1$). This phenomenon is reversed for the lower Z on the obstacle. The

cold flow coming from the lower recirculating zone and the lower horizontal channel (Fig. 8) moves up along the obstacle wall ($Y = 0.90$) before reaching its temperature for $Z \in [0.50, 0.70]$. It then heads again towards the cold plate. Note that the zone ($Y = 0.90$,$Z \in [0.50, 0.70]$) corresponds to the zone where both opposite boundary layer-like flows impinge (Fig. 8).

As for zone A, the temperature of the core of the channel decreases with Z and a thermal stratification is observed. Figure 15 shows the vertical temperature profile in the middle of the unheated channel (Y=0.95, $Z \in [0; 1]$). A linear variation is observed until $Z = 0.5$. For $Z > 0.5$, the vertical temperature gradient is increased. This increase confirms the flow behavior mentioned before and the observed crossing flow through the core of the channel (Fig. 8). In fact, the flow above the division at $Z \approx 0.65$ is hotter because it mainly comes from the top horizontal channel (i.e. zone B).

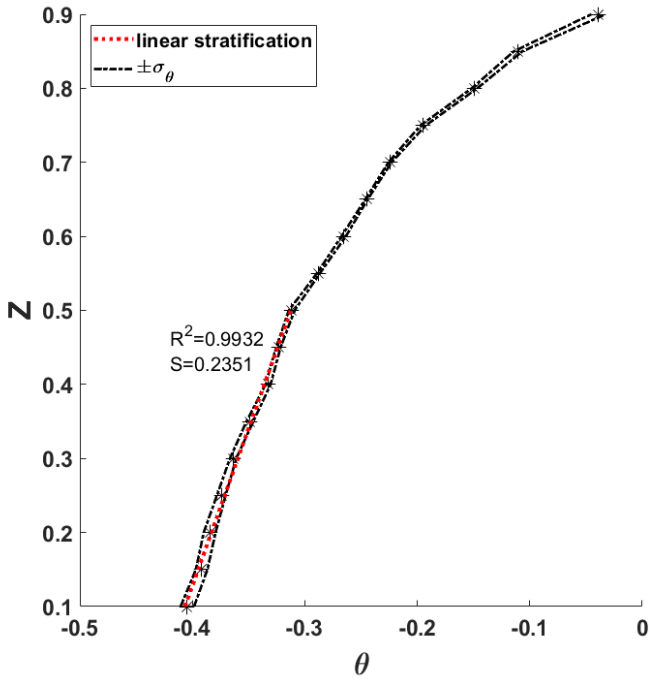

FIGURE 15 – Vertical profile of the mean dimensionless temperature at $Y = 0.95$ for zone C

3.3. Instabilities analysis (zone A)

3.3.1. Low frequency

Occurrence of internal waves in differentially heated cavities has been widely studied [17, 18]. They are found more easily into the stratified cores of the cavities. Thorpe [19] showed that those waves are linked with the Brunt-Väisälä frequency which is defined as :

$$f_{bv} = \frac{1}{2\pi}\sqrt{\frac{g\beta\Delta TS}{L}} \tag{3}$$

For aspect ratios large enough, the frequency of the first modes is approximately equal to f_{bv}. Figure 16 shows the power spectral density for the vertical velocity fluctuation W' ($W' = W_i - W$ where W_i is the instantaneous vertical velocity and W is the vertical mean velocity), at different elevations, Z, in the lower half of the heated channel (zone A). The power spectral density is defined as $\Phi_X = \frac{1}{f_s n_{acq}}|\widehat{X}|^2$ where $\widehat{X}$ is the Fourier transform of the quantity X, f_s is the sampling frequency and n_{acq} is the number of acquisitions. For each Z, a low frequency stands out and fits with the order of magnitude of f_{bv}. Indeed, regarding this study configuration, equation 3 yields $f_{bv} \approx 0.10\,\mathrm{Hz}$.

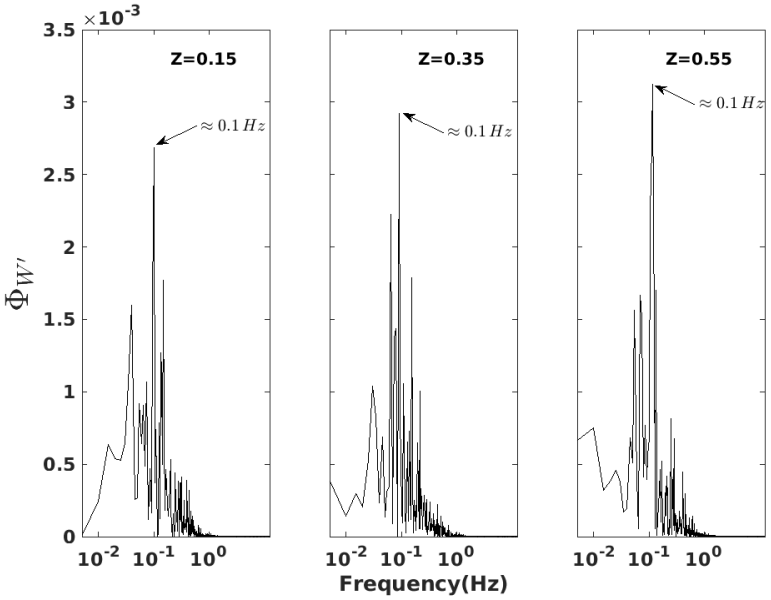

FIGURE 16 – Power spectral density for W' at different Z and $Y = 0.05$

3.3.2. Oscillating buoyant Jet

In zone A, the boundary layer flow leaves the hot plate at $Z = 0.90$ and $Y = 0.10$ inducing a buoyant jet. This buoyant jet oscillates horizontally either towards zone A or zone B (Fig. 17).

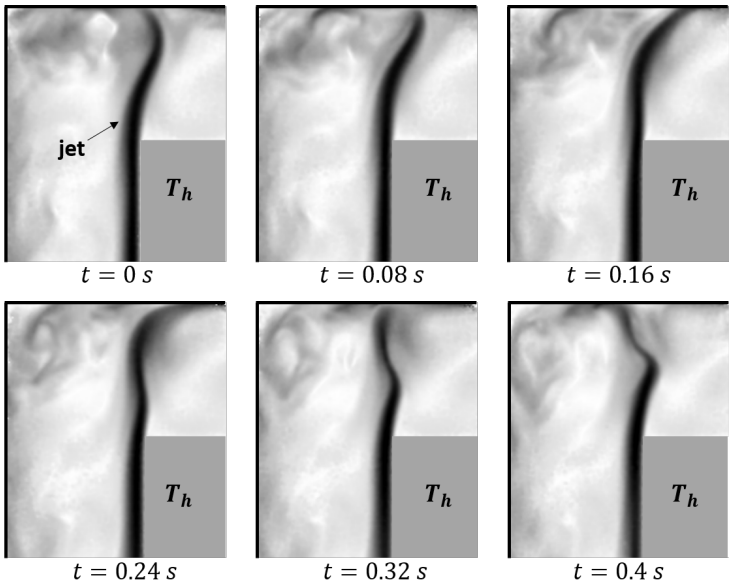

FIGURE 17 – Norm of the instantaneous velocity. Screenshots are taken at different times around the jet located near the top edge of the heated plate (zone A).

Figure 18 shows the power spectral density of the horizontal fluctuations for a point located in this oscillating jet at $Z = 0.94$ and $Y = 0.09$.

It can be observed from spectral analysis that the value of the main oscillating frequency of this buoyant jet is centered around 2 Hz. This frequency comes from a boundary layer instability that will be studied in the next section (3.3.3). The other smaller frequencies can be attributed to internal gravity waves, studied in the previous section, along with the growing complexity of the flow at this elevation.

Figure 19 shows the mean temperature evolution at different elevations, Z, in and around this oscillating jet. The maximum of the mean temperature is to be found into the jet for $Z = 0.901$ (just above the obstacle top corner) and for $Y \approx 0.098$. This maximum decreases with Z increasing. In fact, when the jet leaves the hot plate, the flow is not heated anymore and the jet progressively widens. The jet flattens until $Z = 0.983$ where it drives the flow

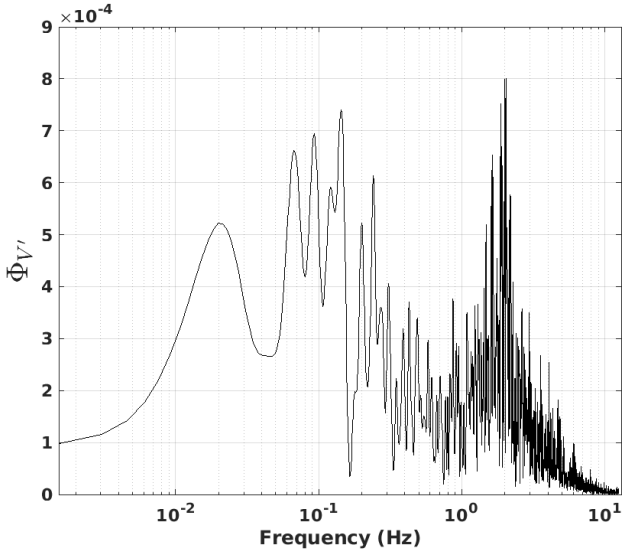

FIGURE 18 – Power spectral density for V' at $Z = 0.94$ and $Y = 0.09$ (located in the oscillating buoyant jet)

either towards the horizontal channel or towards the cold plate (as shown in Fig. 6).

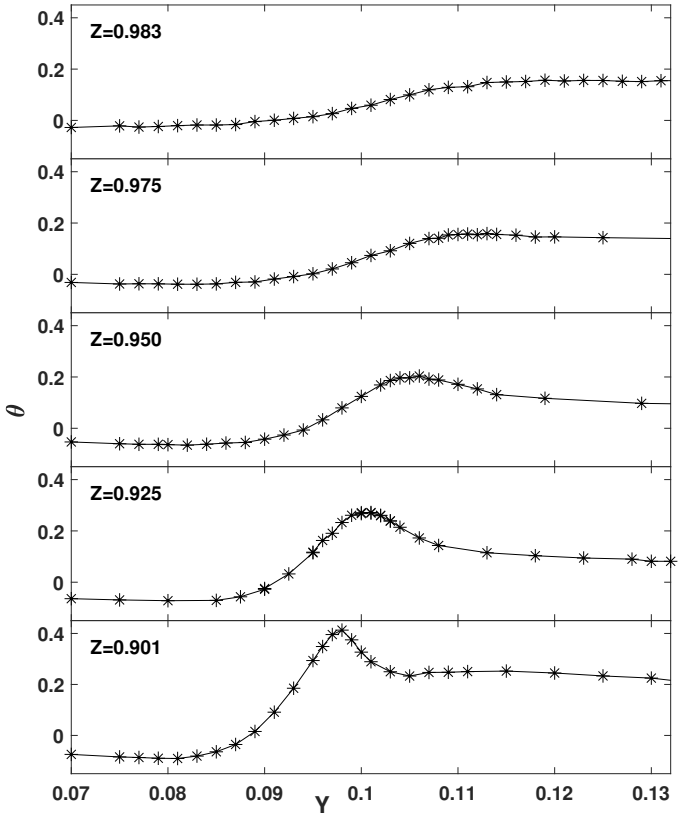

FIGURE 19 – Mean temperature centered around the jet at different elevations Z

3.3.3. Boundary layer instability

The occurrence of a frequency was observed both into the jet and the hot boundary layer flow. The power spectral density of the horizontal velocity fluctuation V' at $Z = 0.65$ and $Y = 0.09$ (Fig. 20) enables to identify this frequency which is approximately equal to 2 Hz.

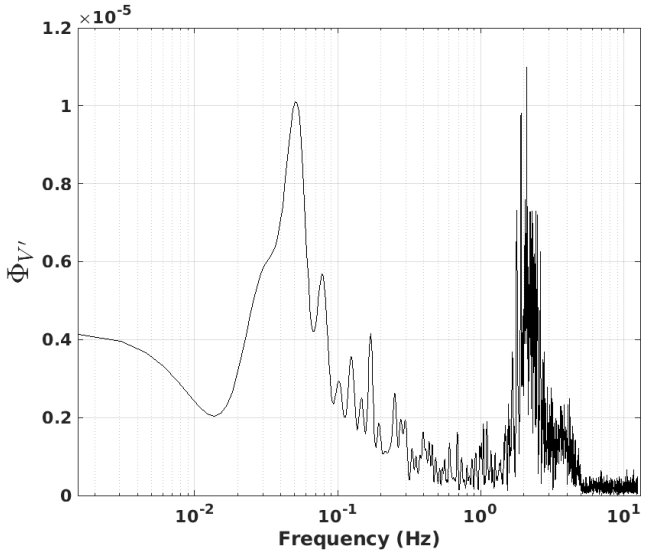

FIGURE 20 – Power spectral density for V' at $Z = 0.65$ and $Y = 0.09$

Gebhart and Jaluria [16] extensively studied the evolution of a propagating downstream periodic wave along heated vertical plates with both isothermal or uniform heat flux surface conditions. Solving the Orr-Sommerfield equations, Dring and Gebhart [3] showed that this periodic wave is amplified downstream and filtered into a single frequency. It will be later confirmed experimentally by Mahajan and Gebhart [20] and Qureshi and Gebhart [21]. This frequency value does not depend on the position along the vertical plate and Gebhart and Jaluria [16] proposed this characteristic pulsation :

$$\Omega = \frac{2\pi f}{\nu}\left(\frac{\nu^2}{g\beta\Delta T^*}\right)^{2/3} \tag{4}$$

where ΔT^* is the temperature difference between the plate temperature and the temperature far away from it. With numerous numerical and experimental results (Hieber and Gebhart [22], Polymeropoulos and Gebhart [23],

Godaux and Gebhart [24]), Gebhart and Mahajan [25] were able to draw asymptotic Prandtl-dependant solutions, in particular for $Pr \in [0.1, 100]$:

$$\Omega = 0.315 Pr^{-0.065} \tag{5}$$

More recently, developing perturbations along isothermal vertical plates were studied by Zhao et al. [26, 27, 28, 29]. They have also observed a growing perturbation of high frequency (that does not depend on the vertical position along the plate) which is acknowledged as the characteristic frequency. For $Pr = 0.7$, they obtained the following correlation for the dimensional characteristic frequency (Hz) :

$$f_c = 0.07 \left(\frac{g\beta\Delta T^*}{\alpha} \right)^{2/3} \nu^{1/3} \tag{6}$$

This correlation can be rewritten according to Gebhart's definition of the dimensionless characteristic pulsation :

$$\Omega = 2\pi \times 0.07 Pr^{2/3} \tag{7}$$

Table 2 shows the characteristic pulsation determined asymptotically by Gebhart (Eq. 5), the one determined by Zhao (Eq. 6) for $Pr = 0.7$ and the one from the present study (Eq. 4). In our case, ΔT^* is the temperature difference between the temperature plate and the mean temperature in the center of the heated channel between $Z = 0.10$ and $Z = 0.90$ (Fig. 11). This temperature choice is motivated by the horizontal shape of the temperature profiles in the cavity center (Fig. 10) and it appears here to be a suitable way to define ΔT^* with respect to Gebhart's definition. Although configurations slightly differ, the pulsation obtained is close to the ones obtained by Gebhart and Zhao and differs only by a maximum of 11%. Furthermore, a possible range for Ω can be determined which takes into account the stratified medium and is $\Omega \in [0.31; 0.47]$.

From the spectral analysis of the velocity fluctuations, the amplitude A_z of the oscillating frequency can be obtained. Figure 21 shows the normalized amplitude of the oscillating frequency obtained at $Y = 0.09$ for several elevations Z. This amplitude is normalized by the assumed neutral amplitude of the oscillating frequency along the vertical plate A_0. The neutral amplitude chosen here, is the amplitude where the disturbance is first detected ($Z_0 \approx 0.4$). The spectrum amplitude is determined with an fft algorithm

	Ω
Gebhart [25]	0.32
Zhao [28]	0.35
present study	0.36

TABLE 2 – Comparison of the characteristic pulsation Ω (Eqs. 4, 5 and 6) for $Pr = 0.71$ and $f = 2\,\mathrm{Hz}$

applied on the normalized horizontal velocity fluctuations ($v'/U_c(z)$) with $U_c(z) = \sqrt{g\beta\Delta T^*(z-0.1)}$ (here 0.1 refers to the elevation of the heated plate leading edge). $U_c(z)$ allows to account for the fluctuations growth induced by the base flow (Dring and Gebhart [3]).

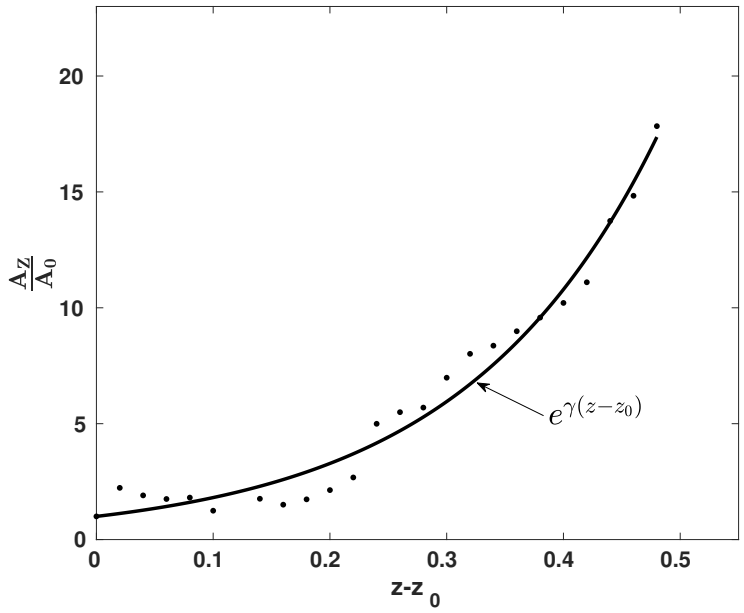

FIGURE 21 – Disturbance amplitude evolution. (.) experimental data ; (–) exponential fitted curve ($\gamma \approx 6$)

There is a quite good agreement with the linear stability theory which predicts [3] :

$$\frac{A_z}{A_0} = e^{-\int_{z_0}^{z} \alpha_i \, dz} \tag{8}$$

where A_0 is the disturbance neutral amplitude, A_Z the disturbance amplitude at Z farther downstream and α_i the spatial amplification rate of the disturbance. Note that the theory predicts the amplitude evolution for an injected perturbation. In our case, the neutral amplitude chosen is only based on observation and cannot be accurately the neutral amplitude described by the theory [30]. However, the criterion used for denoting the instability of the flow is $\alpha_i < 0$. For increasing Z, the criterion in the present study is then respected and leads to an unstable flow in the hot boundary layer and its vicinity.

Considering enclosed spaces, Janssen and Henkes [31, 32], Le Quéré and Behnia [17] and Kishor et al. [33] likewise observed the occurrence of travelling waves inside differentially heated cavities with multiple aspect ratios and angles. In particular, Xin and le Quéré [34] provided critical angular frequencies for the most unstable modes in differentially heated cavities with vertical aspect ratio between 1 and 8. Their results show travelling waves frequencies which are of the same order of magnitude than the one observed in the present study. Those frequencies are determined for a critical Rayleigh number which is one order smaller than the one of the present case. It can be added that the high frequency in the present study does not stand out in the cold boundary layer while it does and stays identical in the differentially heated cavities for any aspect ratios.

3.3.4. Turbulence

The understanding of turbulence development is still a challenge. This is why different ways to describe it have been carried out over the years. One of them is based on the behavior of the fluctuations spectra. Over a heated vertical plate, during the transition to turbulence, the spectrum is centered around the boundary layer characteristic frequency defined earlier. The turbulence developing downstream leads to an energy distribution from large to smaller scales. Considering the frequencies, it means that their is an upper broadening of the fluctuations spectra [35]. Figure 22 shows the cumulative power spectra of three points taken along the hot boundary layer, at $Y = 0.09$.

For the point located at the beginning of the transition (at $Z \approx 0.50$) almost all the energy is concentrated into frequencies smaller than the filtered frequency (2 Hz). During the transition, at $Z = 0.65$, there is a slight broadening around the characteristic frequency meaning that there is a start of energy distribution to the neighbouring frequencies. Farther downstream, at

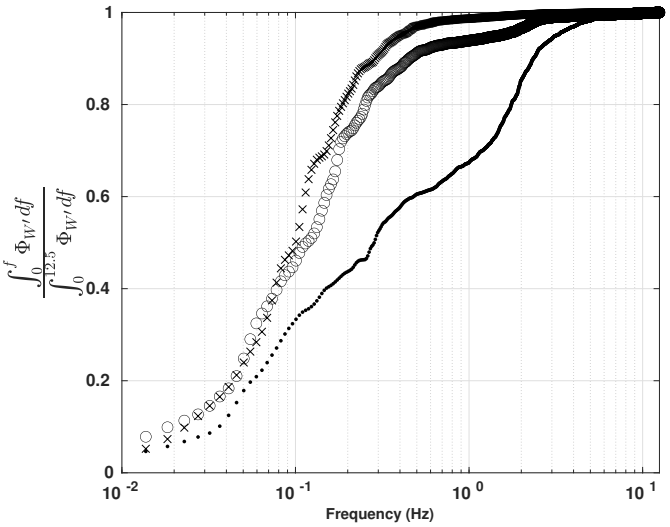

FIGURE 22 – Cumulative power spectra for W'. (•) datas at $Z = 0.80$; (○) $Z = 0.65$; (×) $Z = 0.50$

$Z = 0.80$, the energy is more widely distributed over a large frequency range. In particular, a substantial increase of the energy distribution for frequencies greater than the filtered frequency is observed. It means that the energy has been transferred from large eddies to smaller ones. Moreover, a large part of the energy is still concentrated around the filtered frequency (the gradient around 2 Hz is higher than for smaller frequencies). While the spectrum is broadening, it means that the process of selective frequency amplification still remains. Through the developing spectrum, an "inertial subrange" can arise. It means that the gradient of the spectral density remains constant over a certain range of wave numbers. Lumley [36] showed that it is possible to substitute the wave numbers by the frequencies for small enough turbulence scales and velocity gradients. Considering buoyancy-driven flows, it has been shown that the power spectral density decays with a slope of -3 for a quite large frequency range [16]. Figures 23 and 24 show the power spectral density versus the frequency for two points downstream along the hot plate ($Y = 0.1$). At $Z = 0.65$, during the transition, the energy decay towards frequencies superior to the filtered frequency is non-linear. On the contrary, at $Z = 0.80$, a slope of -3 is observed which confirms the presence of a large inertial subrange starting near the characteristic frequency which is also the

start of the upper frequencies broadening.

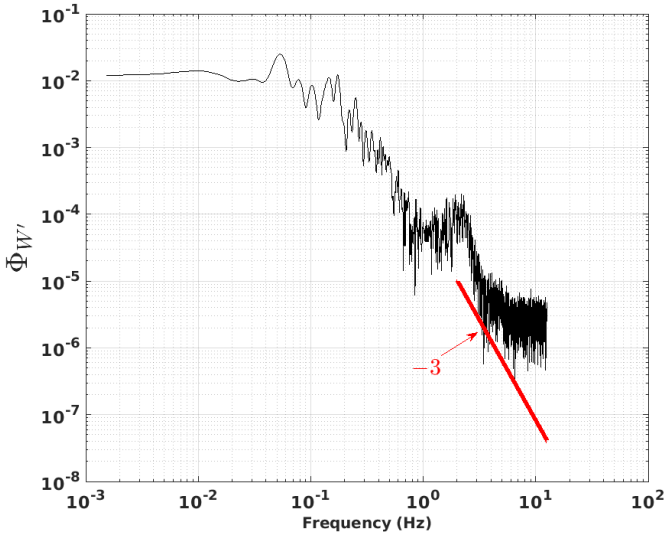

FIGURE 23 – Power spectral density for W' at $Z = 0.65$ and $Y = 0.09$

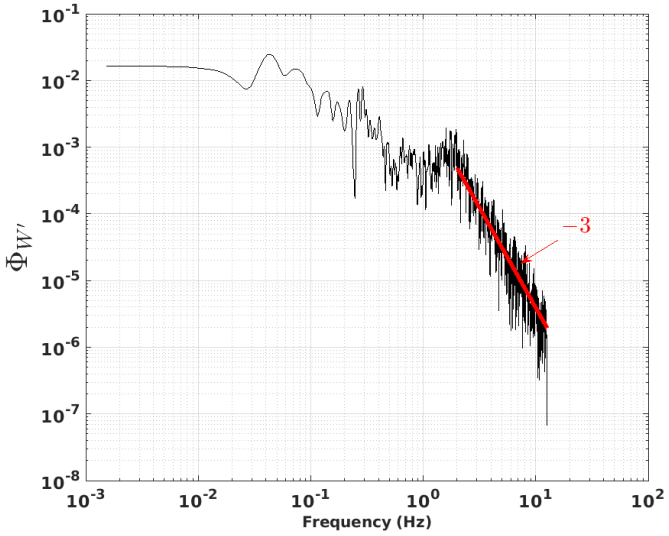

FIGURE 24 – Power spectral density for W' at $Z = 0.8$ and $Y = 0.09$

4. Conclusions and perspectives

We have studied a turbulent natural convection flow whose Rayleigh number is similar to those encountered in industrial applications like the underhood of cars. Understanding the complex flow behavior around an inner heated obstacle in an enclosed space is a crucial issue for industries which rely on optimized heat transfers to ensure their materials thermal resistance.

The dynamical and thermal behavior of a flow in an enclosed cavity with a partially heated obstacle is studied in the work. The heated channel is thermally stratified and a recirculating zone is observed in its upper part. The recirculating zone disturbs the linearity of the stratification and the heat transfers on both the hot and cold plates. Leaving the heated plate of the obstacle, the flow takes the form of an oscillating jet. The occurrence of a travelling wave along the heated plate and internal gravity waves in the core of the heated channel is shown. The boundary layer instability frequency is a of Tollmien-Schlichting type and has been found experimentally around 2 Hz. It is in good agreement with the linear stability theory on a heated vertical plate. Remarkably, this is also the frequency of the oscillating jet.

The gravity wave frequency is approximately equal to the Brunt-Väisälä frequency. Turbulence develops downstream with an upper broadening of the fluctuation spectrum over the travelling wave frequency. An inertial zone of -3 slope appears over the filtered frequency.

It is worth mentioning that data provided in this paper can be useful for further validations of numerical codes used when turbulent flows where dominant buoyancy forces are encountered. In addition, the boundary conditions considered in this study are stationary. A perspective for this investigation is to apply unsteady boundary conditions to the heated plate. Actually, this could help to simulate unsteady cases encountered in industrial systems as car engines, after for instance a sudden stop of the car, when the engine is no longer cooled by a forced external flow.

Acknowledgments

The authors would thank the ANR MONCACO_2025 grant (ANR-17-CE06-0005) for supporting this work as well as the "transport" CPER/FEDER Program. The authors would also like to thank H. Arlaud who built micro-thermocouples and the experimental set-up as well as J.-C. Fraudeau, N. Papin and C. Fuentes for her support with laser techniques.

Appendix

Vertical profiles of the mean horizontal dimensionless velocity in the center of the heated channel ($Y = 0.05$) and in the center of the unheated channel ($Y = 0.095$) are plotted on figure 25.

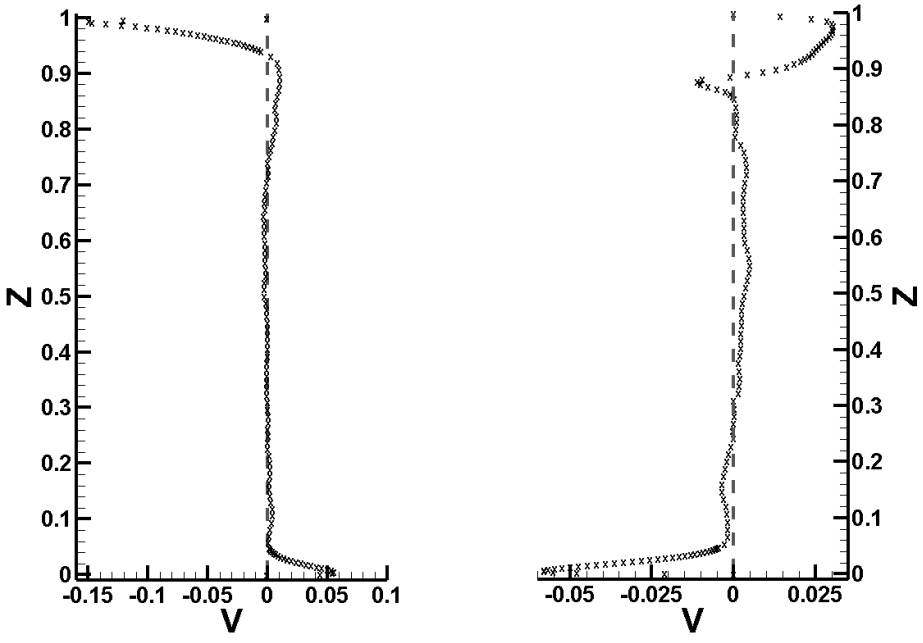

(a) at $Y = 0.05$ (zone A)

(b) at $Y = 0.95$ (zone C)

FIGURE 25 – Vertical profiles of the mean dimensionless horizontal velocity in the center of both the heated and unheated channels (zone A and C)

Références

[1] E. Schmidt and W. Beckmann, "Das temperatur- und geschwindigkeitsfeld vor einer wärme abgebenden senkrechten platte bei natürlicher konvektion," *Technische Mechanik und Thermodynamik*, vol. 1, no. 11, pp. 391–406, 1930.

[2] S. Ostrach, L. F. P. Laboratory, and U. S. N. A. C. for Aeronautics, *An Analysis of Laminar Free-convection Flow and Heat Transfer about*

a Flat Plate Parallel to the Direction of the Generating Body Force. AD-a380 480, National Advisory Committee for Aeronautics, 1952.

[3] R. P. Dring and B. Gebhart, "A theoretical investigation of disturbance amplification in external laminar natural convection," *Journal of Fluid Mechanics*, vol. 34, no. 3, pp. 551–564, 1968.

[4] Y. Jaluria and B. Gebhart, "On transition mechanisms in vertical natural convection flow," *Journal of Fluid Mechanics*, vol. 66, no. 2, pp. 309–337, 1974.

[5] S. Mergui and F. Penot, "Analyse des vitesse et température de l'air en convection naturelle dans une cavité carrée différentiellement chauffée à $ra = 1.69 * 10^9$," *International Journal of Heat and Mass Transfer*, vol. 40, no. 14, pp. 3427–3441, 1997.

[6] J. Salat, S. Xin, P. Joubert, A. Sergent, F. Penot, and P. Le Quéré, "Experimental and numerical investigation of turbulent natural convection in a large air-filled cavity," *International Journal of Heat and Fluid Flow*, vol. 25, pp. 824–832, Oct. 2004.

[7] P. Belleoud, D. Saury, and D. Lemonnier, "Coupled velocity and temperature measurements in an air-filled differentially heated cavity at $ra = 1.2 * 10^{11}$," *International Journal of Thermal Sciences*, vol. 123, pp. 151–161, 2018.

[8] P. Belleoud, *Etude de la convection naturelle turbulente en cavité verticale différentiellement chauffée : Analyse des structures et des transferts turbulents*. phdthesis, ISAE-ENSMA Ecole Nationale Supérieure de Mécanique et d'Aérotechique - Poitiers, 2016.

[9] F. X. Trias, M. Soria, A. Oliva, and C. D. Pérez-Segarra, "Direct numerical simulations of two- and three-dimensional turbulent natural convection flows in a differentially heated cavity of aspect ratio 4," *Journal of Fluid Mechanics*, vol. 586, pp. 259–293, 2007.

[10] J. M. House, C. Beckermann, and T. F. Smith, "Effect of a centered conducting body on natural convection heat transfer in an enclosure," *Numerical Heat Transfer, Part A : Applications*, vol. 18, no. 2, pp. 213–225, 1990.

[11] P. Bhave, A. Narasimhan, and D. A. S. Rees, "Natural convection heat transfer enhancement using adiabatic block : Optimal block size and prandtl number effect," *International Journal of Heat and Mass Transfer*, vol. 49, pp. 3807–3818, Oct. 2006.

[12] Z. A. Raizah, S. E. Ahmed, and A. M. Aly, "Isph simulations of natural convection flow in e-enclosure filled with a nanofluid including homogeneous/heterogeneous porous media and solid particles," *International Journal of Heat and Mass Transfer*, vol. 160, p. 120153, 2020.

[13] A. M. Aly, "Mixing between solid and fluid particles during natural convection flow of a nanofluid-filled h-shaped cavity with three center gates using isph method," *International Journal of Heat and Mass Transfer*, vol. 157, p. 119803, 2020.

[14] Y. Liu and N. Phan-Thien, "A complete conjugate conduction convection and radiation problem for a heated block in a vertical differentially heated square enclosure," *Computational Mechanics*, vol. 24, no. 3, pp. 175–186, 1999.

[15] M. Y. Ha and M. J. Jung, "A numerical study on three-dimensional conjugate heat transfer of natural convection and conduction in a differentially heated cubic enclosure with a heat-generating cubic conducting body," *International Journal of Heat and Mass Transfer*, vol. 43, pp. 4229–4248, Dec. 2000.

[16] B. Gebhart and Y. Jaluria, *Buoyancy-Induced Flows And Transport*. Taylor & Francis, Jan. 1988.

[17] P. Le Quéré and M. Behnia, "From onset of unsteadiness to chaos in a differentially heated square cavity," *Journal of Fluid Mechanics*, vol. 359, pp. 81–107, Mar. 1998.

[18] P. Chorin, F. Moreau, and D. Saury, "Heat transfer enhancement of a natural convection flow in an enclosure submitted to a small extent thermal disturbance : Influence of location and frequency," *International Journal of Thermal Sciences*, vol. 161, p. 106711, Mar. 2021.

[19] S. A. Thorpe, "On standing internal gravity waves of finite amplitude," vol. 32, no. 3, pp. 489–528.

[20] R. L. Mahajan and B. Gebhart, "An experimental determination of transition limits in a vertical natural convection flow adjacent to a surface," *Journal of Fluid Mechanics*, vol. 91, pp. 131–154, Mar. 1979.

[21] Z. H. Qureshi and B. Gebhart, "Transition and transport in a buoyancy driven flow in water adjacent to a vertical uniform flux surface," *International Journal of Heat and Mass Transfer*, vol. 21, pp. 1467–1479, Dec. 1978.

[22] C. A. Hieber and B. Gebhart, "Stability of vertical natural convection boundary layers : some numerical solutions," *Journal of Fluid Mechanics*, vol. 48, pp. 625–646, Aug. 1971.

[23] C. E. Polymeropoulos and B. Gebhart, "Incipient instability in free convection laminar boundary layers," *Journal of Fluid Mechanics*, vol. 30, pp. 225–239, Nov. 1967.

[24] F. Godaux and B. Gebhart, "An experimental study of the transition of natural convection flow adjacent to a vertical surface," *International Journal of Heat and Mass Transfer*, vol. 17, pp. 93–107, Jan. 1974.

[25] B. Gebhart and R. Mahajan, "Characteristic disturbance frequency in vertical natural convection flow," *International Journal of Heat and Mass Transfer*, vol. 18, pp. 1143–1148, Oct. 1975.

[26] Y. Zhao, C. Lei, and J. C. Patterson, "Resonance of the thermal boundary layer adjacent to an isothermally heated vertical surface," vol. 724, pp. 305–336, 2013.

[27] Y. Zhao, C. Lei, and J. C. Patterson, "A PIV measurement of the natural transition of a natural convection boundary layer," vol. 56, no. 1, p. 9, 2015.

[28] Y. Zhao, P. Zhao, Y. Liu, Y. Xu, and J. F. Torres, "On the selection of perturbations for thermal boundary layer control," vol. 31, no. 10, p. 104102, 2019.

[29] Y. Fan, Y. Zhao, J. F. Torres, F. Xu, C. Lei, Y. Li, and J. Carmeliet, "Natural convection over vertical and horizontal heated flat surfaces : A review of recent progress focusing on underpinnings and implications for

heat transfer and environmental applications," vol. 33, no. 10, p. 101301, 2021.

[30] C. P. Knowles and B. Gebhart, "The stability of the laminar natural convection boundary layer," *Journal of Fluid Mechanics*, vol. 34, no. 4, pp. 657–686, 1968.

[31] R. J. A. Janssen and R. a. W. M. Henkes, "Instabilities in three-dimensional differentially-heated cavities with adiabatic horizontal walls," vol. 8, no. 1, pp. 62–74.

[32] R. J. A. Janssen and R. a. W. M. Henkes, "Influence of Prandtl number on instability mechanisms and transition in a differentially heated square cavity," *Journal of Fluid Mechanics*, vol. 290, pp. 319–344, May 1995.

[33] V. Kishor, S. Singh, and A. Srivastava, "Flow instabilities and heat transfer in a differentially heated cavity placed at varying inclination angles : Non-intrusive measurements," *Physics of Fluids*, vol. 33, no. 094103, 2021.

[34] S. Xin and P. L. Quéré, "Natural-Convection Flows in Air-Filled, Differentially Heated Cavities with Adiabatic Horizontal Walls," *Numerical Heat Transfer, Part A : Applications*, vol. 50, pp. 437–466, July 2006.

[35] R. G. Bill and B. Gebhart, "The development of turbulent transport in a vertical natural convection boundary layer," *International Journal of Heat and Mass Transfer*, vol. 22, pp. 267–277, Feb. 1979.

[36] J. L. Lumley, "Interpretation of Time Spectra Measured in High-Intensity Shear Flows," *The Physics of Fluids*, vol. 8, pp. 1056–1062, June 1965.